ARTICLE IN PRESS

Catalysis Today xxx (xxxx) xxx–xxx

Contents lists available at ScienceDirect

Catalysis Today

journal homepage: www.elsevier.com/locate/cattod

Coordination tailoring towards efficient single-atom catalysts for N_2 fixation: A case study of iron-nitrogen-carbon (Fe@N-C) systems

Xiangyu Guo[a], Jinxing Gu[b], Xuemin Hu[c], Shengli Zhang[c,*], Zhongfang Chen[b,*], Shiping Huang[a,*]

[a] State Key Laboratory of Organic-Inorganic Composites, Beijing University of Chemical Technology, Beijing 100029, China
[b] Department of Chemistry, University of Puerto Rico, Rio Piedras, San Juan, PR 00931, USA
[c] MIIT Key Laboratory of Advanced Display Materials and Devices, Ministry of Industry and Information Technology, Institute of Optoelectronics & Nanomaterials, Nanjing University of Science and Technology, Nanjing, 210094, China

ARTICLE INFO

Keywords:
Density functional theory (DFT)
N_2 fixation
Single-atom catalyst

ABSTRACT

N_2 fixation using electrochemical methods offers a promising strategy for NH_3 production. However, it remains a grand challenge to efficiently produce NH_3 in large scale due to the low activity and poor selectivity of the current electrocatalysts. Herein, by means of density functional theory (DFT) computations, we systematically explored the great potential of two-dimensional (2D) single-atom catalysts (SACs), namely carbon-based iron-nitrogen systems (Fe@N_x, x = 0–4) for N_2 electroreduction. Significantly, the catalytic activity and selectivity of Fe@N_x systems are influenced by the coordination environment of single Fe atom. Among all the proposed configurations, Fe@N_2-op, in which two N atoms are located at the opposite coordination sites of single Fe atom, exhibits the highest activity and selectivity for N_2 electroreduction, with a limiting potential of −0.63 V. By examining the scaling relations for the single vacancy and double vacancy-based SACs, we constructed a volcano plot to describe the catalytic activity of carbon-based SACs and proposed an optimal nitrogen adsorption energy for N_2 electroreduction. This work calls for more attention to the coordination effect to the single-atom active site, and helps provide guidance for further developing more effective carbon-based SACs for N_2 fixation.

1. Introduction

Ammonia (NH_3) is not only essential for producing various chemicals, like fertilizers, but also is an important carbon-free energy carrier and energy storage intermediate [1–3]. Nowadays, increasing amount of NH_3 is required to meet the growing needs of economic development. Thus, it is of great importance to develop a sustainable and effective strategy to produce NH_3 from N_2 by the so-called N_2 fixation process [4–6]. Industrial N_2 fixation is currently dominated by the traditional Haber-Bosch process, which requires extreme reaction conditions and consumes large quantity of energy. On the contrary, electrochemical N_2 reduction reaction (NRR), which can be performed at ambient conditions using energy from renewable solar and wind sources, is regarded as a green and sustainable strategy for N_2 fixation. However, NRR in aqueous media has some elementary steps with high reaction barriers and is competed by hydrogen evolution reaction (HER), which lead to low activity and poor selectivity on the electrocatalysts. Nevertheless, tremendous efforts have been devoted to improving the yield of NH_3, such as developing more effective NRR electrocatalysts [7,8] and using non-aqueous electrolytes [9,10].

NRR requires catalysts with specific electronic structures that could activate N_2 and bind intermediates not too weak nor too strong [11,12]. By first principles computations, Nørskov and co-workers found volcano plots between the nitrogen adsorption energy and the catalytic activity of various metal surfaces [13,14]. And several metals, such as Ru, Rh, Mo, and Fe, have been identified as potential catalysts. Particularly, Fe and Fe-based electrocatalysts have attracted much attention due to the potential high catalytic activity, along with its low cost and abundance [15]. However, even though the metal Fe is near the top of the volcano plot, the sizable overpotential and sluggish rates associated with NRR are limiting its application as NRR electrocatalyst. Thus, it is highly desirable to tune the electronic properties of Fe-based electrocatalysts to improve their activity and selectivity for N_2 reduction.

The emerging single-atom catalysts (SACs), which have dispersed single atoms supported on substrates, such as two-dimensional (2D) graphene [16–18], C_3N_4 [19,20], MoS_2 [21] and BN [22] monolayers, provide the possibility to explore the relationship between structure and catalytic activity. Especially, with high electrical conductivity and excellent chemical stability, metal-nitrogen-doped (M@N_x) carbons represent a unique class of SACs, and caught great attentions [23–26].

* Corresponding authors.
E-mail addresses: zhangslvip@njust.edu.cn (S. Zhang), zhongfangchen@gmail.com, zhongfang.chen1@upr.edu (Z. Chen), huangsp@mail.buct.edu.cn (S. Huang).

https://doi.org/10.1016/j.cattod.2019.06.014
Received 11 February 2019; Received in revised form 21 May 2019; Accepted 2 June 2019

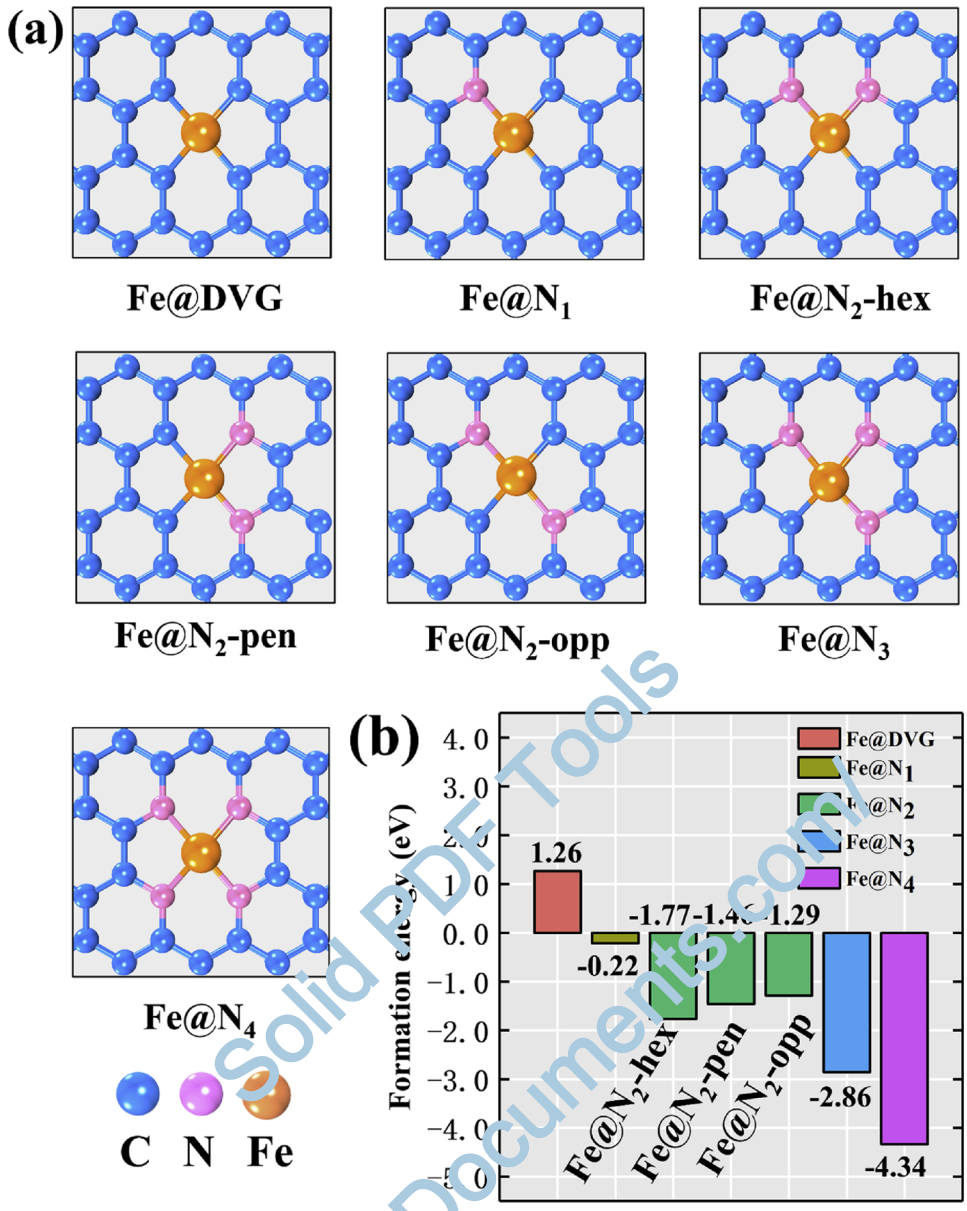

Fig. 1. (a) Geometric structures of single Fe atom embedded in double vacancy graphene and N-doped double vacancy graphene (Fe@N_x, x = 0–4). (b) The calculated formation energy (E_f) of Fe@N_x systems.

Recently, a series of M@N_x moieties have been successfully anchored on graphene monolayer using different methods such as wet-chemical routes and mass-selected soft-landing techniques [27–32]. Experimental studies revealed that the catalytic activity of M@N_x are strongly correlated with the coordination number [33–35]. Following the experimental synthesis of Fe@N_4 moiety, other types of Fe@N_x moieties have been proposed for catalyzing oxygen reduction reaction (ORR) [36–39] and NRR [40]. Unfortunately, due to the lack of a systematical study of Fe@N_x systems, the dependence of catalytic activity and selectivity on the coordination environment, which also plays an important role for NRR, remains unclear, and the scaling relations cannot be well used to predict more efficient NRR catalysts.

Herein by means of density functional theory (DFT) computations, we examined a series of SACs with atomically dispersed Fe atom anchored on N-doped 2D graphene monolayer and investigated their catalytic performance towards NRR. Our results revealed that the catalytic activity and selectivity of Fe@N_x are significantly affected by the coordination environment of the single Fe atom. Fe@N_2-opp moiety, in which two N atoms are located at the opposite coordination sites of the single Fe atom, presents the highest catalytic activity and selectivity. On the basis of linear scaling relation, we also constructed an activity volcano plot using well-described adsorption energy of nitrogen atom (ΔE_{N^*}), which helps guide further design of carbon-based SACs for N_2 fixation.

2. Computational methods

All the spin-polarized DFT computations were performed using the Vienna ab initio simulation package (VASP) [41]. A kinetic energy cutoff of 400 eV was used for plane wave expansion. Projector-augmented-wave (PAW) potentials [42] were employed to represent the electron-ion interactions, and the electron exchange-correlation interactions were treated using generalized gradient approximation (GGA) in the form proposed by Perdew, Burke and Ernzerhof [43]. The dispersion correction was carried out using the DFT-D3 method with the standard parameters programmed by Grimme and co-workers [44].

For adsorption energy calculations, a supercell of 6 × 6 lateral size was used. To avoid artificial interactions between periodic images, the

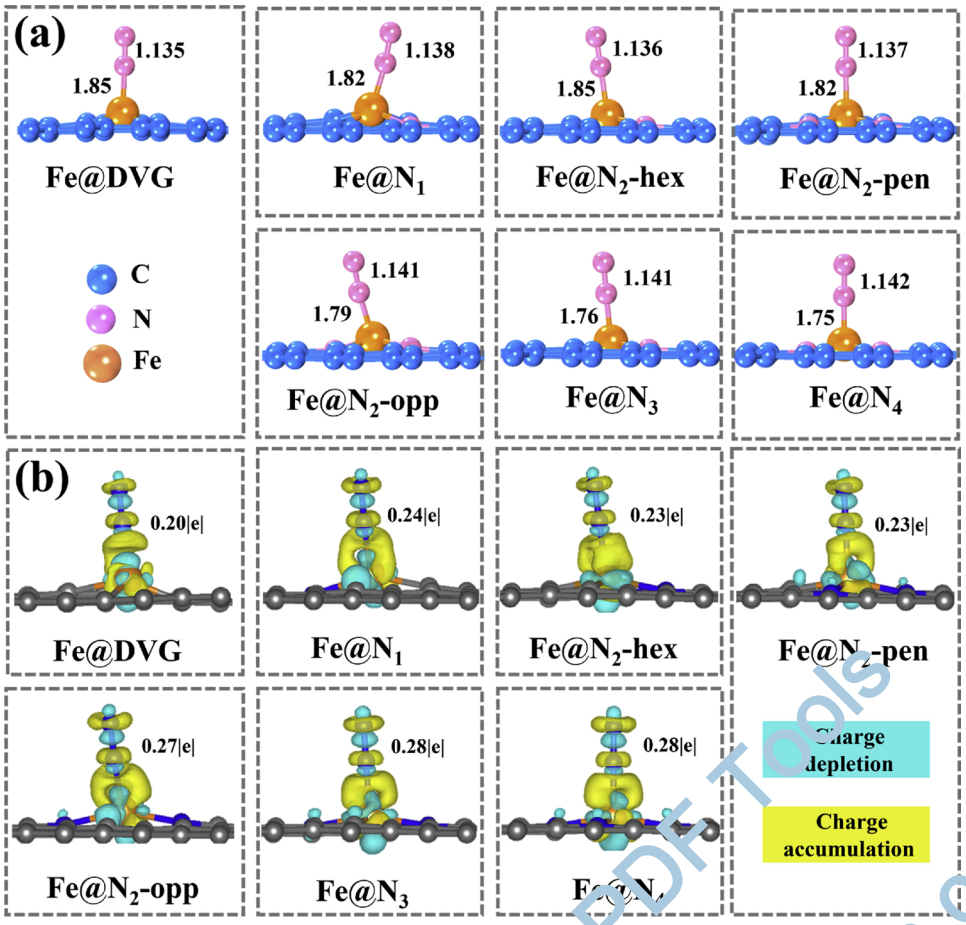

Fig. 2. (a) Optimized structures of N_2 molecules adsorbed on Fe@N_x surfaces. The key bond lengths (Å) are given. (b) Charge density difference for N_2 molecule adsorbed on Fe@N_x surface. The isosurface is set to 0.006 e/Å^3.

interlayer vacuum distance was set to 20 Å. The Brillouin zone was sampled with a 3 × 3 × 1 Monkhorst-Pack k-point grid. Geometry optimizations were carried out using energy and force convergence limits below 10^{-5} eV and 0.02 eV/Å, respectively. The Gibbs free energy of adsorption was corrected from the electronic energy with zero-point energy (ΔZPE) and entropy (ΔS) contributions estimated using the harmonic approximation. For gases, the translational, rotational, and vibrational entropy terms were taken into account, whereas for adsorbates both translational and rotational entropy were neglected. The zero–point energies and entropies of the NRR species were computed from the vibrational frequencies, in which only the adsorbate vibrational modes were calculated explicitly, while the substrate atoms were rigidly constrained. Here, solvation effects were not considered since solvation-induced stabilization of NRR adsorbates are within 0.1 eV [14].

All the Gibbs free energy values for the NRR reaction pathways were referenced to the computational hydrogen electrode (CHE) model as proposed by Nørskov and co-workers [45]. The chemical potential of the H^+/e^- pair is equal to half of the gas-phase H_2 under standard reaction conditions (pH = 0, T = 298.15 K, P = 1 atm)

$$H^+ + e^- \rightleftharpoons 1/2\ H_2\ (g) \quad (1)$$

and the electrode potential was considered by shifting the electron energy by -eU. Thus, the change in Gibbs free energy (ΔG) for each reaction step was given by Eq. (2).

$$\Delta G = \Delta E + \Delta ZPE - T\Delta S - eU \quad (2)$$

The good agreement between the computed thermodynamic quantities for free N_2, H_2, NH_3 molecules with the experimental values (Table S1 of Supporting Information) illustrates the reliability of our DFT computations.

3. Results and discussion

3.1. SAC models and N_2 adsorption

The single Fe atom is embedded in double vacancy graphene (DVG) or N-doped double vacancy graphene, and SACs with different N coordination numbers in the range of 0~4 can be obtained, namely Fe@DVG, Fe@N_1, Fe@N_2, Fe@N_3 and Fe@N_4 (Fig. 1a). Note that there are three possible configurations for the Fe@N_2 system: a) two N atoms at the opposite sides of Fe atom (Fe@N_2-opp), b) Fe and its adjacent N atoms are in the same hexagonal ring (Fe@N_2-hex), and c) two N atoms in the same pentagonal ring (Fe@N_2-pen).

We firstly examined the formation energy (E_f) to evaluate the relative stability of Fe@N_x systems. The E_f was calculated by the equation of $E_f = E_{Fe@N_x} + n\mu_C - (E_{gra} + x\mu_N + E_{Fe})$, where $E_{Fe@N_x}$, E_{gra}, and E_{Fe} are the total energies of Fe@N_x, pristine 6 × 6 graphene supercell, and single Fe atom, respectively. μ_C is the chemical potential of a single C atom in graphene, and μ_N is defined as a half of the nitrogen molecule energy in gas phase. x is the number of N atoms in Fe@N_x systems, and n represents the number of carbon atoms replaced by Fe and N atoms. According to this definition, a lower (more negative) E_f indicates a higher thermodynamic stability of the examined SAC.

As illustrated in Fig. 1b, the E_f values of Fe@N_x systems depend on both doping concentration and doping configuration of N atoms. With increasing the number of coordinated N atoms, the E_f of Fe@N_x systems decreases, leading to the much higher possibility to observe the thermodynamically most favorable Fe@N_4 moiety in experiments. For Fe@N_2 system with three different configurations, Fe@N_2-hex has the lowest formation energy (-1.77 eV), closely followed by Fe@N_2-pen (-1.46 eV) and Fe@N_2-opp (-1.29 eV). Since the Co@N_2-opp and Fe@N_2-opp have been synthesized in experiments [34,36,46], we expect

that the Fe@N_2-hex and Fe@N_2-pen could also be formed under the proper conditions.

We then investigated the adsorption of N_2 molecule on Fe@N_x surfaces in both side-on and end-on configurations. Our computations showed that N_2 prefers adsorption onto the Fe@N_x via end-on configuration (Fig. 2a), with adsorption energies of between −0.41 to −0.60 eV (Table S2). The N≡N bond is elongated from 1.12 Å in a free N_2 molecule to 1.135 ~ 1.142 Å when adsorbed on Fe atom, which is a sign of the N_2 activation. Bader charge analysis revealed that there exist strong charge transfers between the adsorbed N_2 molecules and Fe@N_x surfaces, where N_2 acts as the electron acceptor and the underlying Fe@N_x systems transfer about 0.20 ~ 0.28 |e| to the adsorbed N_2 molecule. Note that the activation of N≡N bond is primarily associated with so-called "acceptance-donation" process in which the metal atom provides unoccupied *d*-orbital to accept electrons from N_2, at the same time, the occupied *d*-orbital of metal atom backdonate electrons into 2π* antibonding orbitals of N_2. The latter process, termed π backdonation, leads to the elongated and electronically depleted N≡N bond. Thus, the bond length of adsorbed N_2 presents an approximately linear relation with the amount of transferred charges (Fig. S1). The charge density difference (Fig. 2b) indicates that upon adsorption, the transferred charges accumulate on 2π* orbital of N_2, resulting in the redistribution of charge density.

3.2. N_2 reduction mechanism

The electrochemical NRR can undergo four possible pathways, named distal [47], alternating [48], enzymatic [49] and mixed mechanisms [50,51]. Since N_2 molecule prefers the end-on adsorption, only distal, alternating and mixed mechanisms (depicted in Fig. 3) were considered to evaluate the catalytic activity of the Fe@N_x systems. Moreover, since the NH_3* can be easily protonated to NH_4^+ and released into solution under the electrochemical conditions [52,53], the further protonation of NH_3^* into NH_4^+ was not considered. The geometric structures of the key intermediates are summarized in Fig. S2, and their Gibbs free energies are listed in Table S3.

According to our computations, all the Fe@N_x systems follow very similar reaction steps. Among them, Fe@N_2-opp exhibits the best catalytic activity towards NRR. Therefore, we take Fe@N_2-opp as the example to elucidate the specific mechanism and the origin of its high activity for N_2 electroreduction.

Fig. 4a presents the free energy diagram of NRR on Fe@N_2-opp. Firstly, a proton coupled with an electron (H^+/e^-) attacks the upper N atom of the adsorbed N_2 molecule. This reaction step is slightly uphill in the free energy profile by 0.63 eV, which indicates that the transfer of the first H^+/e^- pair to the adsorbed N_2 is a nonspontaneous thermodynamic process. Subsequently, the protonation of N_2H^* (or transfer of the H^+/e^-) can proceed via two reaction pathways: (a) $N_2H^* + H^+/e^- \rightarrow NNH_2^*$ (Distal Mechanism) and (b) $N_2H^* + H^+/e^- \rightarrow NHNH^*$ (Alternative mechanism). Comparing the Gibbs free energy change of these two reaction steps, we found that Fe@N_2-opp prefers to catalyze NRR via distal mechanism, since the protonation of N_2H^* to form NNH_2^* intermediate is only 0.04 eV uphill, while the corresponding value for the NHNH* formation is 0.61 eV. Following the distal mechanism, once NNH_2^* is formed, all the other elementary steps are downhill in the Gibbs free energy profile. Further protonation of NNH_2^* leads to the release of the first NH_3 molecule, leaving the N* intermediate on the catalyst surface, and the step is downhill in the free energy profile by 0.26 eV. The remaining N* is continuously hydrogenated to NH*, NH_2^*, and NH_3^*, and the free energy changes for these subsequent steps are −0.26, −0.81 and 0.06 eV, respectively. Finally, the second NH_3 molecule can be desorbed from the Fe@N_2-opp surface after overcoming a positive free energy change of 0.07 eV. Note that for the mixed mechanism, the required energy to protonate NNH_2^* to $NHNH_2^*$ is 0.19 eV, much higher than that of releasing NH_3 following the distal pathway (−0.26 eV). Thus, from the thermodynamic aspect, the distal mechanism could be mostly preferred on the Fe@N_2-opp surface.

The Fe@N_2-opp catalyzed NRR is not spontaneous at a bias potential of 0 V (Fig. 4a, red line). Tuning the bias potential in electrochemical reactions could help overcome the potential barriers. We plotted free energy vs. applied bias potential (Fig. 4b and c) and found that the formation of NNH^* species is the potential determining step (PDS) due to the maximum ΔG values (+0.63 eV) among all the elementary steps. Thus, the limiting potential (U_L), which is the applied potential required to eliminate the energy barrier of PDS, is determined to be −0.63 V following the equation $U_L = -\Delta G/e$, where ΔG is the free energy of PDS.

Hereby, the computed U_L for Fe@N_2-opp is −0.63 V, and the U_L for other systems (Fe@DVG, Fe@N_2-hex, Fe@N_2-pen, Fe@N_3, and Fe@N_4) are −0.98, −0.85, −0.96, −0.78, −0.72, and −1.32 V, respectively. In comparison, the energy barrier of PDS for recently synthesized ruthenium SAC (Ru_1-N_3) is about 0.73 V [54], corresponding to a U_L of −0.73 V. Since the Ru_1-N_3 catalyst exhibited the record-high yield rate (120.9 $\mu g_{NH_3} mg_{cat.}^{-1} h^{-1}$) ever reported, we expect that the more favorable (less negative) U_L (−0.63 V) could render Fe@N_2-opp as a promising candidate for electrochemical N_2 fixation.

3.3. Origin of catalytic activity of Fe@N_x systems

To understand the origin of catalytic activity of Fe@N_x systems, we analyzed the effect of doping concentration and doping configuration of N atoms on limiting potential U_L. The intrinsic NRR activity of Fe@N_x is highly correlated to the doping concentration (Fig. 5a), since the U_L values on Fe@N_x vary significantly with augmenting the N contents. Note that with the same N doping concentration, Fe@N_2 with different configurations also exhibit different activities, confirming the important effect of doping configuration to the catalytic activity.

On the other hand, the first protonation of N_2^* to form N_2H^* is identified as the PDS, which means that the adsorption energy of N_2H^* could be set as a descriptor. We plotted the scaling relation between U_L values and the adsorption energy of N_2H^* ($\Delta E_{N_2H^*}$) (Fig. 5b), and found

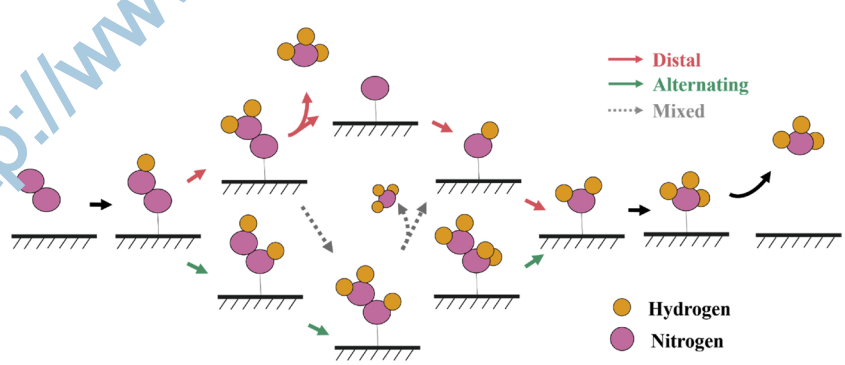

Fig. 3. Schematic illustration of the distal, alternating and mixed mechanisms for NRR on Fe@N_x surfaces.

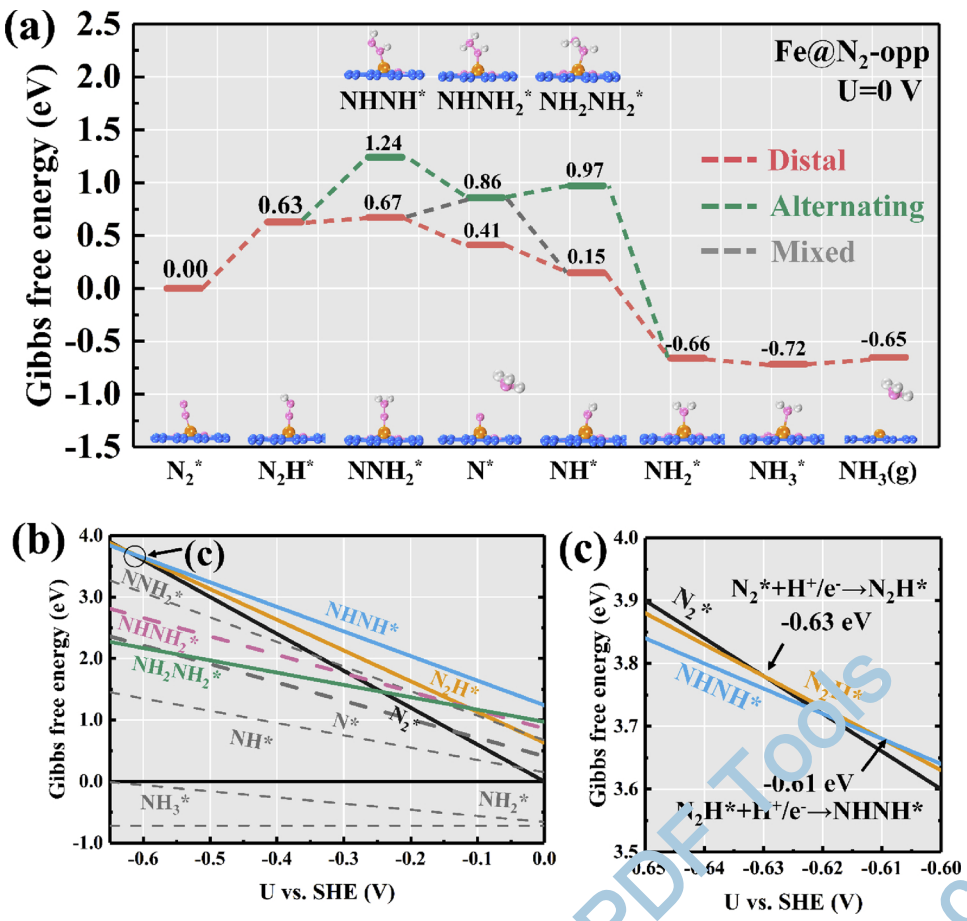

Fig. 4. (a) Gibbs free energy profile for N_2 electroreduction on Fe@N_2-opp surface at zero potential. The bias potential is relative to the standard hydrogen electrode (SHE). Different intermediates following the distal and alternative mechanisms are denoted by red and green lines, respectively. (b) and (c) are the potential-dependent NRR phase diagram for Fe@N_2-opp system. The zero value on the free energy axis is referenced to N_2 and H_2 in gas phase.

a good linear relation, $U_L = -0.98\ \Delta E_{N_2H^*} - 0.86$. Among the SACs under investigation, Fe@N_2-opp exhibits the strongest adsorption ability to N_2H^* and acts as the best catalyst, which agrees with the consensus that the optimal NRR catalyst should selectively stabilize N_2H^* [22].

In general, the different adsorption behaviors of N_2H^* on Fe@N_x can be rationalized by either the charge transfer, a non-covalent interaction, and/or the band hybridization, a covalent interaction. According to Bader charge analysis, there are about 0.21 ~ 0.26 |e| transferred from the substrates to the adsorbed N_2H (Table S4). Checking the relation between $\Delta E_{N_2H^*}$ and the amount of transferred charge (Fig. S2) revealed that no good linear relationship exists between $\Delta E_{N_2H^*}$ and the transferred charge, suggesting that covalent interaction between the N_2H intermediate and attached single Fe atom could play a more important role in N_2H adsorption.

Thus, we examined the partial density of states (PDOS) of N_2H adsorbed on Fe@N_x surface (Fig. 6). The 2π and 3σ orbitals of N_2H intermediate strongly hybridize with the Fe-3*d* band, forming bonding states below the Fermi level. Note that for the $2\pi^*$ antibonding orbital, the band hybridization is significantly affected by the substrates, leading to partial occupation of the formed *d*-$2\pi^*$ orbitals.

To further elucidate the bonding nature of the N_2H intermediate, we

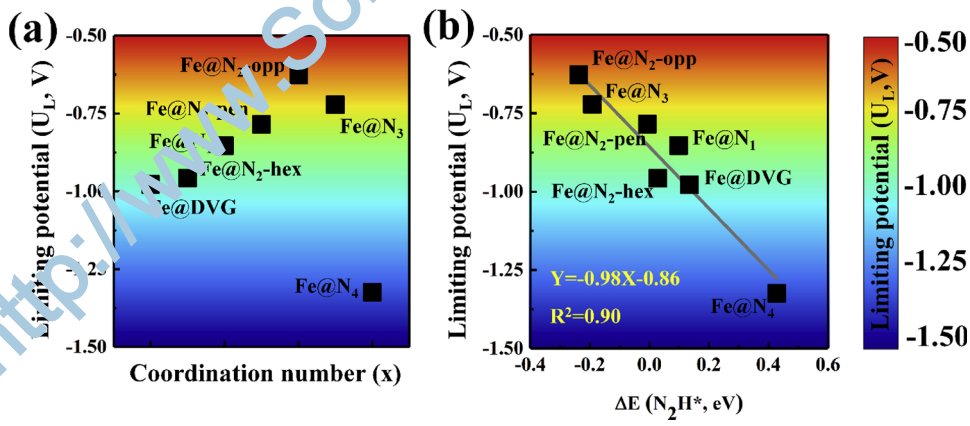

Fig. 5. (a) Calculated limiting potential U_L for nitrogen reduction reaction (NRR) on Fe@N_x surfaces. (b)The scaling relation for limiting potential U_L versus the adsorption energy of N_2H^* ($\Delta E_{N_2H^*}$).

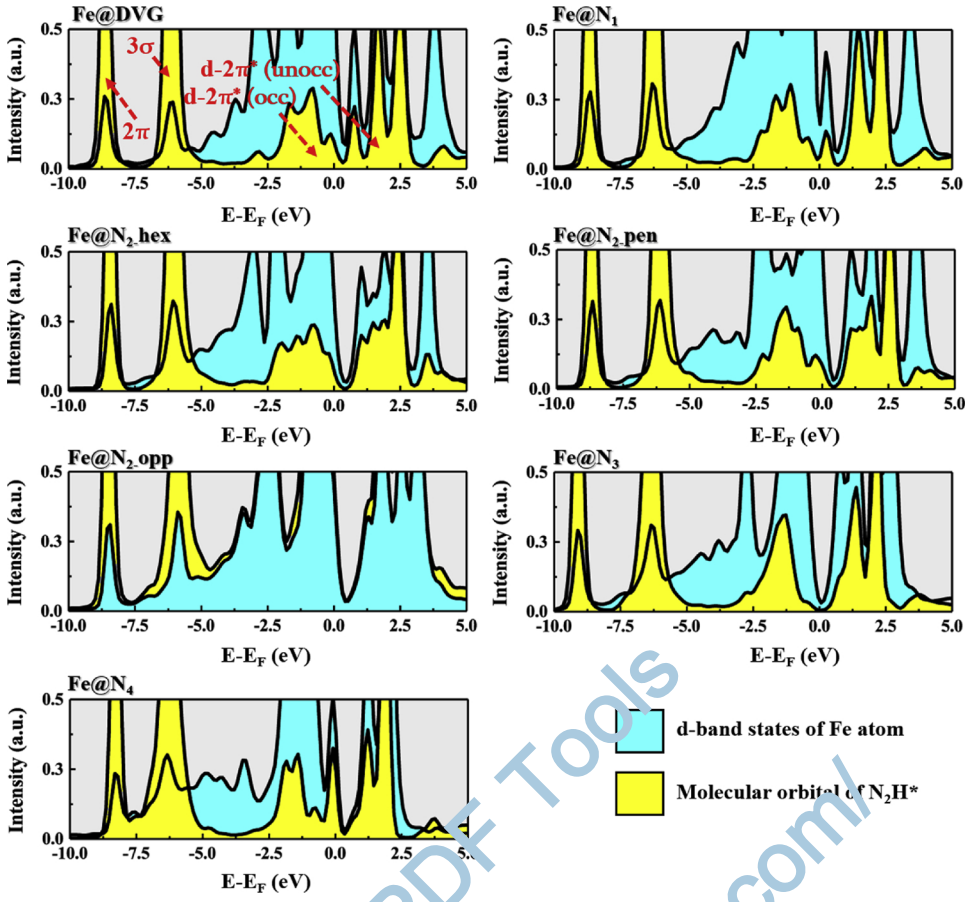

Fig. 6. Calculated partial density of states (PDOS) of N_2H intermediate adsorbed on Fe@N_x surface. The Fermi level is set to 0 eV.

examined the bonding and antibonding states of N_2H adsorbed on Fe@N_x by crystal orbital Hamilton population (COHP) analysis [55,56]. Fig. 7a presents the -COHP curves of the covalent N-H/Fe interaction in the adsorption configurations. The N_2H adsorption is characterized by massively bonding states below the Fermi level, whereas the antibonding states are found above the Fermi level. Clearly the $2\pi^*$ of N_2H^* are partially occupied. Integrating the -COHP up to the Fermi level gives a bonding energy (-ICOHP). Interestingly, the $\Delta E_{N_2H^*}$ values have a rather good linear relation with the -ICOHP ($R^2 = 0.84$), as shown in Fig. 7b. Note that a more negative -ICOHP value indicates a stronger covalent interaction between N_2H and Fe atom, which benefits the adsorption of N_2H intermediate and decreases of the potential barrier of NRR.

Notably, though Fe@N_4 displays superior ability in π backdonation to N_2, its interaction with N_2H^*, which determines the limiting potential, is not that strong. This can be well understood by checking its -ICOHP value. Fe@N_4 displays a more positive value relative to other Fe@N_x systems (Fig. 7), which indicates a weaker binding between N_2H^* and Fe atom. As a result, the N_2H^*, an important reaction intermediate in N_2 reduction, presents low stability on Fe@N_4, thus resulting in the poor catalytic performance for N_2 reduction.

Overall, we proposed that a COHP analysis can be used to quantitatively describe the orbital hybridization, which highlights the important role of the partially occupied *d*-$2\pi^*$ state of N_2H^* in the adsorption of N_2H intermediate.

3.4. Catalytic selectivity of Fe@N_x for NRR

After studying the catalytic activity of Fe@N_x for NRR, it is important to consider the competing hydrogen evolution reaction (HER) during the whole NRR process in aqueous media, since the HER might greatly impede the Faradaic efficiency.

Thus, we computed the free energy diagram of HER on Fe@N_x (Fig. 8a, for detailed adsorption configurations and Gibbs free energies, see Fig. S4). For Fe@DVG surface, due to the strong interaction between the H atom and catalyst surface, the HER process is limited by H* adsorption step ($H^* + (H^+/e^-) \rightarrow H_2(g)$) with a Gibbs free energy change of 0.23 eV. In contrast, the HER process is limited by the H atom adsorption step ($H^+/e^- \rightarrow H^*$) on the N-doped analogues: for Fe@N_1, Fe@N_2, Fe@N_3 and Fe@N_4 systems, and the HER potential barriers are 0.22, 0.34, 0.13, 0.45, 0.29 and 0.38 eV, respectively. Thus, by applying a bias potential of −0.13 to −0.45 V, the H adsorption free energy can go downhill, and the H_2 production can be feasible. Among Fe@N_x systems, Fe@N_2-opp presents the highest potential barrier for HER, indicating that Fe@N_2-opp could suppress HER during the N_2 electroreduction process, and the selectivity limitation is the least severe.

Moreover, previous investigations showed that the catalytic selectivity of NRR/CO_2RR can be estimated by the difference between the limiting potentials for NRR/CO_2RR and HER [14,16,57,58]. Thus, we examined the difference between the limiting potentials for NRR and HER (U_L(NRR) – U_L(HER)) to evaluate the catalytic selectivity of Fe@N_x, (Fig. 8b). The less negative value of U_L(NRR) – U_L(HER) corresponds to higher selectivity towards NRR. Significantly, the computed U_L(NRR) – U_L(HER) value for Fe@N_2-opp is only −0.18 V, which is much better than that of metal-based benchmark (ca. −0.5 V) [14]. We also investigated the free energy diagram of HER on Ru_1-N_3 (see Fig. S5). The U_L(NRR) – U_L(HER) value for Ru_1-N_3 (−0.43 V) is more negative than that of Fe@N_2-opp (−0.18 V), which suggests that Fe@N_2-opp has a better selectivity towards NRR than Ru_1-N_3. Thus, the high catalytic activity (as reflected by the NRR limiting potential) and selectivity render Fe@N_2-opp as the most distinguished NRR electrocatalyst.

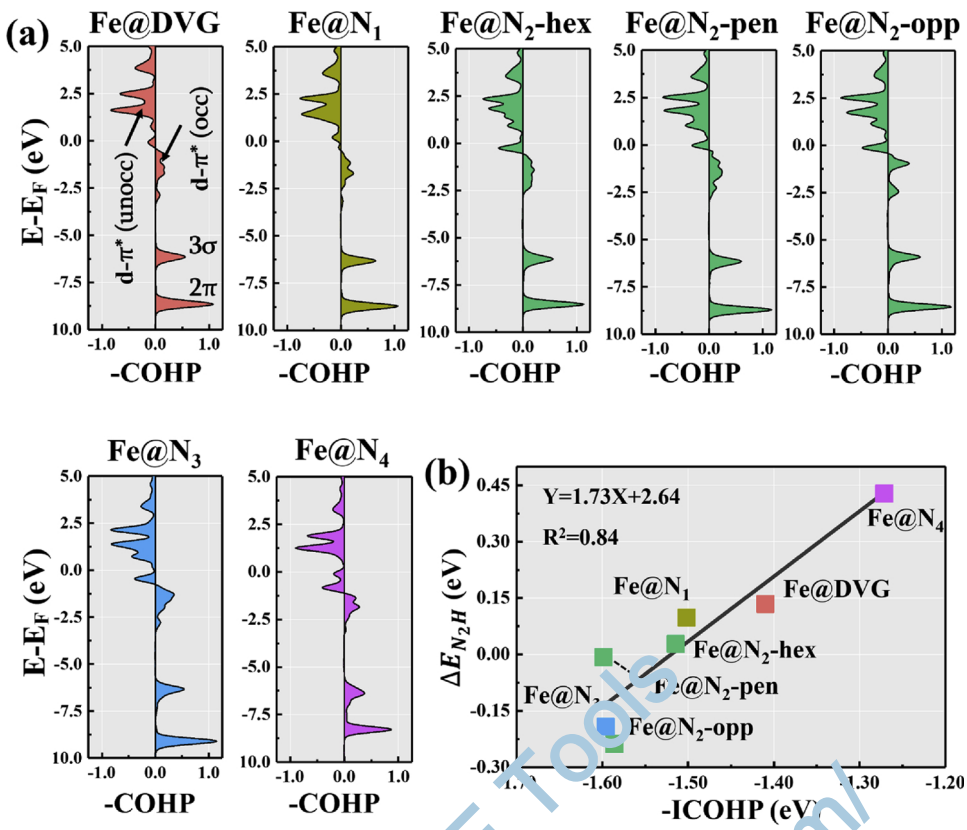

Fig. 7. (a) Crystal orbital Hamilton population (COHP) bonding analysis of N_2H adsorbed on Fe@N_x. The bonding and antibonding interactions between the N_2H and single Fe atom are shown in the right and left sides of the diagram, respectively. (b) Calculated -ICOHP versus $\Delta E_{N_2H^*}$ for N_2H adsorbed on Fe@N_x.

3.5. Prospect for designing the carbon-based SACs

Usually, the Gibbs free energies for the adsorption of nitrogen and nitrogen-involving intermediates on various metal surfaces change in the same direction. This phenomenon is known as scaling relation between the nitrogen containing intermediates [13,14]. Using the adsorption energy of nitrogen atom(ΔE_{N^*}) as the activity descriptor, previous studies proposed a scaling relationship between the ΔE_{N^*} and the limiting potential U_L, and identified three crucial elementary steps for NRR: a) the reductive adsorption of N_2 to form N_2H^*, b) the NH_2 protonation to form NH_2^*, and c) the desorption of NH_2^* to form NH_3 molecule. However, the scaling relations available in the literature have been established primarily on close-packed (111), (211) and (110) metal surfaces, the dependence of these relations on SACs remains unexplored. Here, we developed potentially far-reaching scaling relations by using the ΔE_{N^*} to help select the best SAC for N_2 fixation.

Fig. 9 displays the volcano plot of theoretical limiting potential U_L as a function of ΔE_{N^*} for the Fe@N_x systems. As a comparison, the catalytic activities of single Fe atom embedded in single vacancy and N-doped single vacancy graphene, namely Fe@SVG, Fe@N_1-SV, Fe@N_2-SV, and Fe@N_3-SV, are also plotted (for details, see Table S6 and Figs. S6-7). Clearly, SACs that bind nitrogen too weakly are limited by the adsorption of N_2 to form N_2H^* in the first NRR elementary step, whereas those with too strong binding are limited by either the protonation of NH* to form NH_2^* or the desorption of NH_2^* to form NH_3 molecule.

For single vacancy-based SACs (single Fe atom embedded in single vacancy and N-doped single vacancy graphene), the central Fe metal

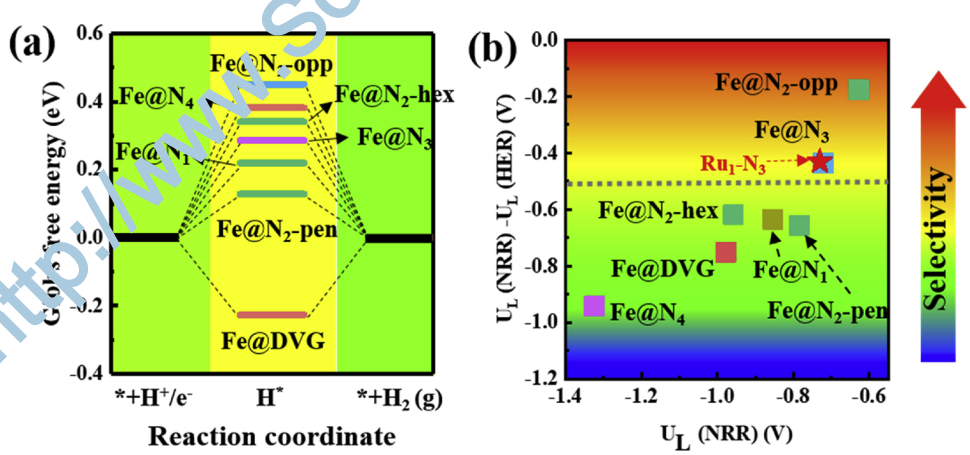

Fig. 8. (a) The free energy diagram of hydrogen evolution reaction on Fe@N_x surfaces. (b) The difference between the limiting potentials for NRR and HER (U_L(NRR) – U_L(HER)) versus U_L(NRR). In comparison, the corresponding value for Ru_1-N_3 is highlighted by asterisk.

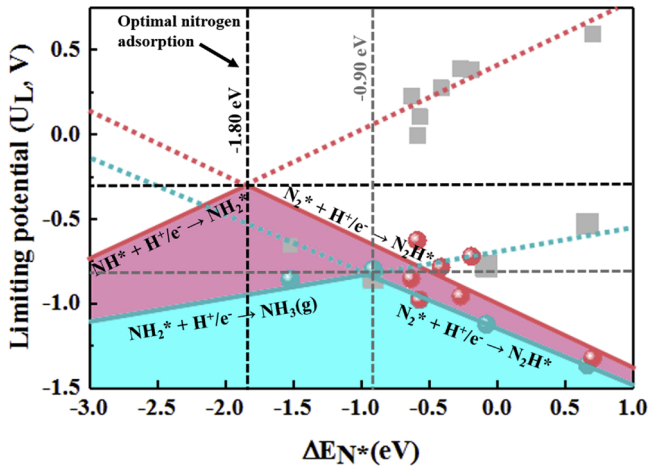

Fig. 9. Activity volcano plot of limiting potential (U_L) for N_2 reduction as a function of ΔE_{N*}. The scaling relations for the single vacancy and double vacancy-based single-atom catalysts are depicted by cyan and red, respectively. The ΔE_{N*} is calculated by the equation: $\Delta E_{N^*} = E_{N^*} - E_* + E_{NH_3} - E_{N_2} - 3/2 * E_{H_2}$, where the E_{N^*} and E_* are the total energies of catalyst with and without the adsorbed nitrogen atom, E_{NH_3}, E_{N_2} and E_{H_2} are the total energies of free NH_3, N_2 and H_2, respectively.

atom combines with three neighboring atoms, forming the non-planar $M@N_x$ moiety (Fig. S6). The decreased coordination number results in more unoccupied orbitals of the metal atom, which provides an extra degree of stabilization for the NH_2* intermediate. We found that the optimal ΔE_{N*} for these single vacancy-based SACs should be about −0.90 eV. When ΔE_{N*} is less than −0.90 eV, NRR could be limited by the desorption of NH_2* to form NH_3 molecule, resulting in low yield rates for NH_3 production.

On the other hand, the metal atom at double vacancies (our studied $Fe@N_x$ systems) allows intermediates to interact with support plane due to the less protrusion of the metal atom. The approximately planar configuration and decreased unoccupied orbitals of the metal atom reduce the binding strength of NH* and NH_2*, favoring the removal of NH_2* as NH_3. Hence, the optimal activity towards NRR occurs when the binding strength of nitrogen is neither too strongly nor too weakly, which can balance the formation of N_2H* and the protonation of NH*. The optimal ΔE_{N*} for the double vacancy-based single-atom catalysts is found to be around −1.80 eV, and the corresponding liming potential is estimated by −0.30 V. This result has been demonstrated by a recent work [1], as $V@N_4$, and $V@N_3$-DVG displayed the excellent performance with U_L of −0.41, and −0.35 V, respectively [59].

4. Conclusions

In summary, by means of systematic DFT computations, we showed that rationally modifying particular physicochemical characteristics of carbon-based two-dimensional SACs can help achieve NRR catalysts with performance exceeding the metal based benchmark. We identified that $Fe@N_2$-opp moiety, in which two N atoms are at the opposite sides of a single Fe atom, has a high catalytic activity for NRR with a limiting potential of −0.63 V. Especially, $Fe@N_2$-opp can also well suppress HER during the N_2 electroreduction process, and has the highest selectivity for NRR among all of the considered $Fe@N_x$ moieties. Furthermore, based on the linear scaling relations, we proposed a design strategy to optimize the catalytic activity of carbon-based SACs for NRR. Our computations suggest that the limiting potential of divacancy-based SACs can be further reduced by tuning the adsorption energy of nitrogen atom, and SACs with ca. -1.80 eV nitrogen atom adsorption energy could have even higher NRR catalytic activity. This study highlights that controlling the coordination environment of the single metal atom is an important method to achieve high performance SACs, and provides guidelines to further improve the activities of the carbon-based single-atom catalysts for N_2 fixation.

Acknowledgments

This work is supported in China by the National Natural Science Foundation of China (Grant No. 21776004), the Fundamental Research Funds for the Central Universities (No. 30916015106) and in USA by the National Science Foundation-Centers of Research Excellence in Science and Technology (NSF-CREST Center) for Innovation, Research and Education in Environmental Nanotechnology (CIRE2N) (Grant No. HRD-1736093) and NASA (Grant No. 80NSSC17M0047). This research used resources of the High Performance of Computational facility (HPCf), University of Puerto Rico, which is partially supported by an Institutional Development Award (IDeA) INBRE Grant Number P20GM103475 from the National Institute of General Medical Sciences (NIGMS), a component of the National Institutes of Health (NIH), and the Bioinformatics Research Core of the INBRE. Its contents are solely the responsibility of the authors and do not necessarily represent the official view of NIH. A portion of this research used computational resources at the Center for Nanophase Materials Sciences, which is a DOE Office of Science User Facility.

Appendix A. Supplementary data

Supplementary material related to this article can be found, in the online version, at doi:https://doi.org/10.1016/j.cattod.2019.06.014.

References

[1] J.G. Chen, R.M. Crooks, L.C. Seefeldt, K.L. Bren, R.M. Bullock, M.Y. Darensbourg, P.L. Holland, B. Hoffman, M.J. Janik, A.K. Jones, M.G. Kanatzidis, P. King, K.M. Lancaster, S.V. Lymar, P. Pfromm, W.F. Schneider, R.R. Schrock, Science 360 (2018) 6611.
[2] S.L. Foster, S.I.P. Bakovic, R.D. Duda, S. Maheshwari, R.D. Milton, S.D. Minteer, M.J. Janik, J.N. Renner, L.F. Greenlee, Nat. Catal. 1 (2018) 490–500.
[3] J. Guo, P. Chen, Chem 3 (2017) 709–712.
[4] A.R. Singh, J.H. Montoya, B.A. Rohr, C. Tsai, A. Vojvodic, J.K. Nørskov, ACS Catal. 8 (2018) 4017–4024.
[5] C. Guo, J. Ran, A. Vasileff, S.Z. Qiao, Energy Environ. Sci. 11 (2018) 45–56.
[6] C.S.M. van der Ham, M.T.M. Koper, D.G.H. Hetterscheid, Chem. Soc. Rev. 43 (2014) 5183–5191.
[7] D. Bao, Q. Zhang, F.L. Meng, H.X. Zhong, M.M. Shi, Y. Zhang, J.M. Yan, Q. Jiang, X.B. Zhang, Adv. Mater. 29 (2017) 1604799.
[8] M. Nazemi, S.R. Panikkanvalappil, M.A. El-Sayed, Nano Energy 49 (2018) 316–323.
[9] B.L. Sheets, G.G. Botte, Chem. Commun. 54 (2018) 4250–4253.
[10] B.H.R. Suryanto, C.S.M. Kang, D. Wang, C. Xiao, F. Zhou, L.M. Azofra, L. Cavallo, X. Zhang, D.R. MacFarlane, ACS Energy Lett. 3 (2018) 1219–1224.
[11] Z.W. Seh, J. Kibsgaard, C.F. Dickens, I. Chorkendorff, J.K. Nørskov, T.F. Jaramillo, Science 355 (2017) 4998.
[12] Y. Wang, W. Qiu, E. Song, F. Gu, Z. Zheng, X. Zhao, Y. Zhao, J. Liu, W. Zhang, Sci. Rev. 5 (2017) 327–341.
[13] E. Skulason, T. Bligaard, S. Gudmundsdottir, F. Studt, J. Rossmeisl, F. Abild-Pedersen, T. Vegge, H. Jonsson, J.K. Norskov, Phys. Chem. Chem. Phys. 14 (2012) 1235–1245.
[14] J.H. Montoya, C. Tsai, A. Vojvodic, J.K. Nørskov, ChemSusChem 8 (2015) 2180–2186.
[15] B. Cui, J. Zhang, S. Liu, X. Liu, W. Xiang, L. Liu, H. Xin, M.J. Lefler, S. Licht, Green Chem. 19 (2017) 298–304.
[16] K. Jiang, S. Siahrostami, A.J. Akey, Y. Li, Z. Lu, J. Lattimer, Y. Hu, C. Stokes, M. Gangishetty, G. Chen, Y. Zhou, W. Hill, W.B. Cai, D. Bell, K. Chan, J.K. Nørskov, Y. Cui, H. Wang, Chem 3 (2017) 950–960.
[17] Z. Wang, J. Zhao, J. Wang, C.R. Cabrera, Z. Chen, J. Mater. Chem. 6 (2018) 7547–7556.
[18] X. Guo, S. Huang, Electrochim. Acta 284 (2018) 392–399.
[19] Y. Zheng, Y. Jiao, Y. Zhu, Q. Cai, A. Vasileff, L.H. Li, Y. Han, Y. Chen, S.Z. Qiao, J. Am. Chem. Soc. 139 (2017) 3336–3339.
[20] C. Ling, X. Niu, Q. Li, A. Du, J. Wang, J. Am. Chem. Soc. 140 (2018) 14161–14168.
[21] G. Liu, A.W. Robertson, M.M.J. Li, W.C.H. Kuo, M.T. Darby, M.H. Muhieddine, Y.C. Lin, K. Suenaga, M. Stamatakis, J.H. Warner, S.C.E. Tsang, Nat. Chem. 9 (2017) 810.
[22] J. Zhao, Z. Chen, J. Am. Chem. Soc. 139 (2017) 12480–12487.
[23] Y. Peng, B. Lu, S. Chen, Adv. Mater. (2018) 1801995.
[24] S. Mitchell, E. Vorobyeva, J. Pérez-Ramírez, Angew. Chem. Int. Ed. 57 (2018) 15316–15329.
[25] C. Ling, X. Bai, Y. Ouyang, A. Du, J. Wang, J. Phys. Chem. C 122 (2018)

16842–16847.
[26] T. He, S.K. Matta, A. Du, Phys. Chem. Chem. Phys. 21 (2019) 1546–1551.
[27] W. Chen, J. Pei, C.T. He, J. Wan, H. Ren, Y. Zhu, Y. Wang, J. Dong, S. Tian, W.C. Cheong, S. Lu, L. Zheng, X. Zheng, W. Yan, Z. Zhuang, C. Chen, Q. Peng, D. Wang, Y. Li, Angew. Chem. Int. Ed. 129 (2017) 16302–16306.
[28] J. Xie, J.D. Kammert, N. Kaylor, J.W. Zheng, E. Choi, H.N. Pham, X. Sang, E. Stavitski, K. Attenkofer, R.R. Unocic, A.K. Datye, R.J. Davis, ACS Catal. 8 (2018) 3875–3884.
[29] H. Fei, J. Dong, Y. Feng, C.S. Allen, C. Wan, B. Volosskiy, M. Li, Z. Zhao, Y. Wang, H. Sun, P. An, W. Chen, Z. Guo, C. Lee, D. Chen, I. Shakir, M. Liu, T. Hu, Y. Li, A.I. Kirkland, X. Duan, Y. Huang, Nat. Catal. 1 (2018) 63–72.
[30] H. Wang, Q. Wang, Y. Cheng, K. Li, Y. Yao, Q. Zhang, C. Dong, P. Wang, U. Schwingenschlögl, W. Yang, X.X. Zhang, Nano Lett. 12 (2012) 141–144.
[31] H.J. Qiu, Y. Ito, W. Cong, Y. Tan, P. Liu, A. Hirata, T. Fujita, Z. Tang, M. Chen, Angew. Chem. Int. Ed. 54 (2015) 14031–14035.
[32] Y. Chen, S. Ji, Y. Wang, J. Dong, W. Chen, Z. Li, R. Shen, L. Zheng, Z. Zhuang, D. Wang, Y. Li, Angew. Chem. Int. Ed. 129 (2017) 7041–7045.
[33] P. Yin, T. Yao, Y. Wu, L. Zheng, Y. Lin, W. Liu, H. Ju, J. Zhu, X. Hong, Z. Deng, G. Zhou, S. Wei, Y. Li, Angew. Chem. Int. Ed. 55 (2016) 10800–10805.
[34] X. Wang, Z. Chen, X. Zhao, T. Yao, W. Chen, R. You, C. Zhao, G. Wu, J. Wang, W. Huang, J. Yang, X. Hong, S. Wei, Y. Wu, Y. Li, Angew. Chem. Int. Ed. 130 (2018) 1962–1966.
[35] F. Li, G.F. Han, H.J. Noh, S.J. Kim, H.Y. Jeong, Z. Fu, J.B. Baek, Energy Environ. Sci. 11 (2018) 2263–2269.
[36] H. Shen, E. Gracia-Espino, J. Ma, H. Tang, X. Mamat, T. Wagberg, G. Hu, S. Guo, Nano Energy 35 (2017) 9–16.
[37] H. Tan, Y. Li, X. Jiang, J. Tang, Z. Wang, H. Qian, P. Mei, V. Malgras, Y. Bando, Y. Yamauchi, Nano Energy 36 (2017) 286–294.
[38] C. Santoro, A. Serov, R. Gokhale, S. Rojas-Carbonell, L. Stariha, J. Gordon, K. Artyushkova, P. Atanassov, Appl. Catal. B-Environ. 205 (2017) 24–33.
[39] X. Chen, L. Yu, S. Wang, D. Deng, X. Bao, Nano Energy 32 (2017) 353–358.
[40] X.F. Li, Q.K. Li, J. Cheng, L. Liu, Q. Yan, Y. Wu, X.H. Zhang, Z.Y. Wang, Q. Qiu, Y. Luo, J. Am. Chem. Soc. 138 (2016) 8706–8709.
[41] G. Kresse, J. Furthmüller, Comput. Mater. Sci. 6 (1996) 15–50.
[42] G. Kresse, D. Joubert, Phys. Rev. B 59 (1999) 1758–1775.
[43] J.P. Perdew, K. Burke, M. Ernzerhof, Phys. Rev. Lett. 77 (1996) 3865–3868.
[44] S. Grimme, J. Comput. Chem. 27 (2006) 1787–1799.
[45] J.K. Nørskov, J. Rossmeisl, A. Logadottir, L. Lindqvist, J.R. Kitchin, T. Bligaard, H. Jónsson, J. Phys. Chem. B 108 (2004) 17886–17892.
[46] H.R. Byon, J. Suntivich, Y. Shao-Horn, Chem. Mater. 23 (2011) 3421–3428.
[47] J. Chatt, J.R. Dilworth, R.L. Richards, Chem. Rev. 78 (1978) 589–625.
[48] L.C. Seefeldt, B.M. Hoffman, D.R. Dean, Annu. Rev. Biochem. 78 (2009) 701–722.
[49] B. Hinnemann, J.K. Nørskov, Top. Catal. 37 (2006) 55–70.
[50] J. Rittle, J.C. Peters, J. Am. Chem. Soc. 138 (2016) 4243–4248.
[51] J.S. Anderson, J. Rittle, J.C. Peters, Nature 501 (2013) 84.
[52] H.-J. Chun, V. Apaja, A. Clayborne, K. Honkala, J. Greeley, ACS Catal. 7 (2017) 3869–3882.
[53] V. Rosca, M.T.M. Koper, J. Phys. Chem. B 109 (2005) 16750–16759.
[54] Z. Geng, Y. Liu, X. Kong, P. Li, K. Li, Z. Liu, J. Du, M. Shu, R. Si, J. Zeng, Adv. Mater. (2018) 1803498.
[55] V.L. Deringer, A.L. Tchougréeff, R. Dronskowski, J. Phys. Chem. A 115 (2011) 5461–5466.
[56] S. Maintz, V.L. Deringer, A.L. Tchougréeff, R. Dronskowski, J. Comput. Chem. 37 (2016) 1030–1035.
[57] C. Shi, H.A. Hansen, A.C. Lausche, J.K. Nørskov, Phys. Chem. Chem. Phys. 16 (2014) 4720–4727.
[58] S. Siahrostami, K. Jiang, M. Karamad, K. Chan, H. Wang, J. Nørskov, ACS Sustain. Chem. Eng. 5 (2017) 11080–11085.
[59] C. Ling, Y. Ouyang, Q. Li, X. Bai, X. Mao, A. Du, J. Wang, Small Methods (2018) 1800376.